INTERNATIONAL JOURNAL FOR NUMERICAL METHODS IN FLUIDS
Int. J. Numer. Meth. Fluids 2009; **59**:173–194
Published online 2 June 2008 in Wiley InterScience (www.interscience.wiley.com). DOI: 10.1002/fld.1817

CFD analysis of an oscillating wing at various reduced frequencies

Farooq Umar[1,2,*,†], Hossein Raza Hamdani[2], Anwar-ul-Haque[1], Sajid Raza Chaudhry[1] and Khalid Parvez[2]

[1]*Centres of Excellence in Science and Applied Technologies* (*CESAT*), *P.O. Box 2801*, *Islamabad*, *Pakistan*
[2]*Department of Aerospace Engineering*, *College of Aeronautical Engineering*, *National University of Sciences and Technology* (*NUST*), *Risalpur Campus*, *Risalpur*, *Pakistan*

SUMMARY

The effect of various reduced frequencies has been examined for an oscillating aspect ratio 10 NACA 0015 wing. An unsteady, compressible three-dimensional (3D) Navier–Stokes code based on Beam and Warming algorithm with the Baldwin–Lomax turbulence model has been used. The code is validated for the study against published experimental data. The 3D unsteady flow field is simulated for reduced frequency values of 0.1, 0.2 and 0.3 for a fixed mean angle of attack position and fixed amplitude. The type of motion is sinusoidal harmonic. The force coefficients, pressure distributions and flow visualization show that at the given conditions the flow remains attached to the wing surface even at high angles of attack with no clear separation or typical light-to-deep category of dynamic stall. Increased magnitude of hysteresis and higher gradients are seen at higher reduced frequencies. The 3D effects are even found at midspan locations. In addition, the rate of decrease in lift near the wing tips compared with the wing root is not much like in the static cases. Copyright © 2008 John Wiley & Sons, Ltd.

Received 24 January 2007; Revised 4 March 2008; Accepted 4 March 2008

KEY WORDS: oscillating wing; reduced frequency; dynamic stall; flow separation; CFD

1. INTRODUCTION

In the field of unsteady aerodynamics, the study of dynamic motion of airfoils and wings has been an interest of the researchers for quite some years. Various types of motions have been studied experimentally and numerically, and the effect of various parameters and phenomena involved has been investigated, of which, the oscillating motion and the related phenomenon known as *dynamic stall* (DS) and its various effects have been widely investigated. In the same context, a lot of

*Correspondence to: Farooq Umar, Centres of Excellence in Science and Applied Technologies (CESAT), P.O. Box 2801, Islamabad, Pakistan.
†E-mail: farooqumar6@yahoo.com

research has been focused on controlling this phenomenon. There are many applications related to oscillatory motion and the DS. The airfoils of some aircraft components are frequently subject to rapid periodic changes of α while operating in specific regions of flight envelop. Similarly, the propellers on airplanes flying at very high altitudes and the airplanes having tilting rotors or propellers are subject to the effects of DS. Moreover, it is of interest for researchers working in the field of UAVs' oscillating/flapping wings and missile aerodynamics. Other applications include wind turbine rotors and turbomachinery.

Most of the research in this field has been focused on helicopters. Helicopter rotor blades are heavily loaded and at high forward speeds experience the dynamic effects. Changes in α are periodic and sinusoidal in nature. The performance of a helicopter is basically limited by the compressibility effects on the advancing blade and the effect of DS on the retreating blade. DS occurs when an airfoil or wing is rapidly pitched to an α more than its static stall angle. The temporary lift produced is much more than its static value due to the generation of DS vortex (DSV), which actually delays the separation. This lift is subsequently lost in a highly nonlinear manner once this vortex sheds. The performance enhancements seem possible in the above-mentioned application areas of helicopter rotor blades, turbomachinery, aircraft maneuverability and micro-aerial vehicles, etc. with the desirable characteristics of DS process. DS can be categorized into various stages such as *no stall*, *stall onset*, *light stall* and *deep stall* [1, 2]. There are many factors that make the analysis of oscillatory motion *vis-a-vis* DS a complex one. Airfoil shape, Reynolds number, Mach number, reduced frequency, mean α and amplitude of motion and type of motion are the major factors besides three-dimensional (3D) effects near the wing tips that have a significant effect. The factors such as wing planform shape and its sweep back angle also play an important role.

A lot of experimental work and numerical simulations have been conducted on various motion types and DS in the past for two-dimensional (2D) cases. However, fewer of them can be found in the literature for 3D ones. The phenomenon of the DS was first measured in 1933 by Farren [3], England. He carried out experiments on various 1930s British airfoils. Further notable studies on the phenomenon were carried out during the 1970s, of which worth mentioning is the work of McCroskey *et al.* [4] in 1976 and 1982 [5] and McAlister *et al.* [6] in 1978. Later a lot of experimental and numerical work has been done by various authors where they have investigated this phenomenon from the point of view of its physical mechanics and various factors affecting the DS phenomenon. Most of the recent work in the 1990s is based on the assessment of turbulence models in the study of DS. The reviews by McCroskey *et al.* [4], Carr [7] and Ekaterinaris and Platzer [8] have mentioned the 2D work in detail.

In 3D, Lorber *et al.* [9] and Lorer [10] did detailed experimentation of unsteady flow over unswept and swept wings for a relatively higher Reynolds number of compressible flow. Owing to the transitional Reynolds number, the numerical simulation may pose difficulties. The effects of free stream velocity and reduced frequency were also considered. Schreck and Helin [11] used aspect ratio, AR = 4, NACA 0015 wing at Mach number 0.03. The experimental Reynolds number was 6.9×10^4. Ramp motion was employed for the study. Results were presented for a variety of reduced ramp rates along with detailed surface pressure measurements. Piziali [12] used AR = 5, Semispan NACA 0015 wing at Mach number ≈ 0.3 and $Re = 2 \times 10^6$. The effect of reduced pitch rates is given. In addition, spanwise pressure distribution along with aerodynamic coefficients is provided. Tang and Dowell [13] used AR = 1.5, NACA 0012 wing at Mach number = 0.1 and $Re = 0.52 \times 10^6$. The experiment was carried out below and above the static stall angle in order to identify the onset and evolution of DSV. Coton and Galbraith [14] and Moir and Coton [15] used square wing of AR = 3, NACA 0015 wing at Mach number 0.1 and $Re = 1.3 \times 10^4$ and 1.5×10^6,

DOI: 10.1002/fld

respectively. The type of motion employed was ramp down, ramp up and harmonic oscillations in pitch for various α and pitch rates. Surface pressure measurements and smoke visualizations were conducted. Berton *et al.* [16, 17] used AR = 2.8, NACA 0012 wing at Mach number 0.1 and $Re = 3.73 \times 10^5$. He also employed oscillatory motion. Boundary layer measurements and velocity profiles along with turbulence quantities are provided.

Apart from 3D experimental work, the 3D computational fluid dynamics (CFD) simulations published till now are very few, one of the main reasons being the limitation of adequate computer resources. In 1994, Newsom [18] in the laminar regime and Ekaterinaris [19, 20] in the turbulent regime have carried out the simulation work at various angles of attack and different pitch rates. Similarly, Morgan and Visbal [21] in 2001 have done the simulation on a wing spanning the wind tunnel cross section without any tip exposed to free stream. Recently in 2005, Spentzos *et al.* [22, 23] have published their detailed work focusing mainly on the evolution and interaction of the wing tip vortex and DSV during a ramp-up motion.

2. THE PRESENT STUDY

The CFD tool provides high temporal and spatial information compared with the experiment that requires state-of-the-art visualization techniques. The 3D unsteady viscous simulations were found to give a wealth of results at the expense of considerable amounts of CPU time. This paper attempts in the first instance, in a series of computational studies through code development, its validation and application to study the most complex DS phenomenon from the computational method. This effort would facilitate the research community to find methods of controlling the DSV or inhibiting the formation of DSV or applying modern techniques such as synthetic jet actuators and several others to control the flow.

As already mentioned DS effects occur on the retreating blade of the helicopter rotor motion. The DS loads may shorten the fatigue life of the blades considerably. Different tests have indicated that this phenomenon can induce limit cycle oscillations that result in grounding of the helicopter for replacement of costly components. The oscillations and the stall in addition to the loss of ability to generate lift transmits very large sudden blade pitching moments to the flight control system. To avoid control loads, a stall boundary has to be set for rotor loads and flight speed. Now these imposed limits effect maneuverability and agility.

The advances in the material technology and urge for higher performance have generated interest in the research community for further understanding the phenomenon and its consequences in order to find the solutions and take advantage of it where possible. In the same context, the present study is targeted toward the oscillating motion of helicopter rotor blades. Typical values of Mach number for helicopter rotor is 0.20–0.70 and the Reynolds number is 2–12 million, whereas the reduced frequency values are 0.05–3.5. Although the helicopter industries have mostly used their own airfoils for the rotor blades, it is seen that most of the published experimental and consequently the numerical studies are carried out for NACA 0012 and NACA 0015 airfoils. In addition, excluding the experimental studies of Piziali [12] and Berton *et al.* [16, 17] other studies are mainly concentrated on low to transitional Reynolds numbers. The current study is carried out for a relatively higher AR = 10, NACA 0015 wing with rectangular cross section, zero sweep and twist at high Reynolds number. In this context, the only appropriate case for the validation appears to be the experimental work of Piziali [12]. Three case studies are performed with different reduced frequency values of 0.10, 0.20 and 0.30 for the typical sinusoidal harmonic motion [12, 20] having

DOI: 10.1002/fld

11° mean α position and 4.2° amplitude. The Mach number of 0.299 and the Reynolds number of 2 million are kept constant for all the cases.

3. COMPUTATIONAL METHOD AND GRID GENERATION

The code used in the current study has been developed and validated for a variety of cases over a period of many years [24–34] for 2D and 3D cases. In brief, the governing equations are used in a strong conservation form as mentioned in the literature [35] and are not expressed here. The perfect gas law, Sutherland's viscosity formula, a constant Prandtl number and the algebraic eddy viscosity model for turbulence are used with the equations. The equations are solved using the implicit, approximate factorization algorithm as given by Beam and Warming [36]. The scheme is formulated using a three-point backward implicit time differencing and a second-order finite difference approximation for all spatial derivatives. In order to successfully initiate a computation with approximate starting data and to enhance the stability behavior suppressing the high-frequency oscillations constant coefficient fourth-order explicit and second-order implicit spectral damping [35] terms are added.

3.1. Coordinate transformations for wing motion

The 3D current version of the code has been developed to enable the user to run it for either a static or an oscillating wing for structured grids. Relative grid and flow velocities are computed in the code to accomplish the grid motion. Appropriate transformations are mentioned below. By considering a wing with non-inertial body coordinate system $Ob(Xb, Yb, Zb)$, which carries out motion around an inertial, fixed coordinate system $O(X, Y, Z)$ through angle ψ with radius a, the wing can also pitch up or down in oscillation through angle α (see Figure 1).

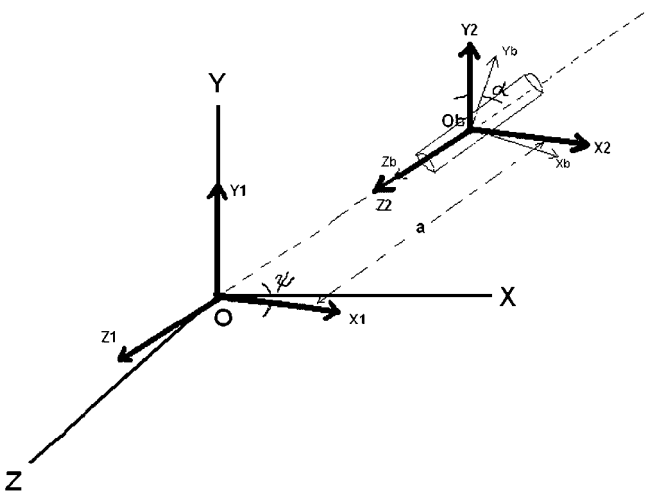

Figure 1. Wing $Ob(Xb, Yb, Zb)$ in hovering motion around a fixed point $O(X, Y, Z)$.

DOI: 10.1002/fld

Considering the oscillatory motion of the wing in pitch only, the coordinate transformation is given as follows:

$$\begin{bmatrix} X \\ Y \\ Z \end{bmatrix} = \begin{bmatrix} \cos\psi\cos\alpha & \cos\psi\sin\alpha & -\sin\psi \\ -\sin\alpha & \cos\alpha & 0 \\ \sin\psi\cos\alpha & \sin\psi\sin\alpha & \cos\psi \end{bmatrix} \begin{bmatrix} Xb \\ Yb \\ Zb \end{bmatrix} - \begin{bmatrix} -a\sin\psi \\ 0 \\ a\cos\psi \end{bmatrix}$$

As $a=0$ and $\psi=0$

$$X = Xb\cos\alpha + Yb\sin\alpha$$

$$Y = -Xb\sin\alpha + Yb\cos\alpha$$

$$Z = Zb$$

also $\alpha=\alpha(t)$, therefore

$$X_t = -Xb\sin\alpha\dot{\alpha} + Yb\cos\alpha\dot{\alpha}$$

$$Y_t = -Xb\cos\alpha\dot{\alpha} - Yb\sin\alpha\dot{\alpha}$$

$$Z_t = 0$$

and

$$V_{X_2} = (V_X - X_t)\cos\alpha + (V_Y - Y_t)\sin\alpha$$

$$V_{Y_2} = (V_X - X_t)\sin\alpha + (V_Y - Y_t)\cos\alpha$$

$$V_{Z_2} = V_Z$$

where V_{X_2}, V_{Y_2} and V_{Z_2} are the relative velocities. The flowchart of the current version of the code is shown in Figure 2.

3.2. Turbulence modeling

The Baldwin–Lomax [37] turbulence model is used in the present code. It is a two-layer model and was made for separated flows and flows with shock waves where the boundary layer thickness, the velocity thickness and the boundary layer edge velocity are difficult to determine. This model has been used by many authors for different types of flow problems to satisfactory levels of success. Being an algebraic model, it uses Boussinesq's eddy viscosity approximation to compute the Reynolds stress tensor as the product of an eddy viscosity and the mean strain rate tensor in terms of mixing length. The model is chosen in the present flow simulations considering its less computational cost being a zero equation model and keeping in view its past success in modeling static stall and DS [28, 29, 31–33, 38], although Ekaterinaris [18, 19] in his study has preferred the Baldwin–Barth [39] model over others including Baldwin–Lomax. In the current simulations in which the flow is expected to be attached or slightly separated, the use of the Baldwin–Lomax model is appropriate. It is important to note that for separated flows, the Baldwin–Lomax model is inappropriate and therefore efforts are under way to include higher-order turbulence models for future work.

DOI: 10.1002/fld

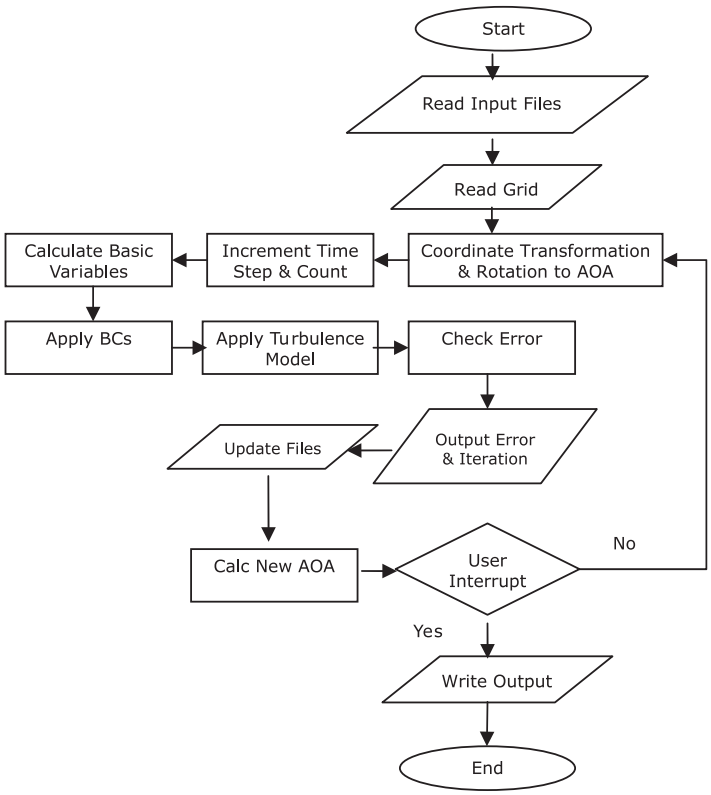

Figure 2. A flowchart.

3.3. Selection of grid and time step

The 3D grid is constructed by spanwise stacking of 2D O-type grids. The resulting topology is an O-H-type grid. The AR = 5, semispan grid is made in order to put more grid points on the wing by using symmetry at the wing root. Care is taken not to make a large size grid that would be computationally intensive and result in wastage of time and resources keeping in view the accuracy of the solution within acceptable limits. The criterion for comparison was chosen to be the force curves as provided in the published experimental work [12]. Various grids used are shown in Table I and Figure 3 shows the effect of various grid sizes on the accuracy of the force coefficients' results. It was established that the fine grid no. 5 (1 252 800 points) gave almost the same results as the finest grid no. 6 (1 800 000 points). Therefore, the need to further refine the grid was not considered. The coarser grids, however, lacked accuracy and could not follow the published results compared with the two finest grids. Therefore, grid no. 5 was chosen for this study. The outer domain is kept at 10 times the chord length. From wing tip to outer extent in the spanwise direction, a distance equal to half-span is kept. The normal distance of the first grid point is 3×10^{-5} times the chord length in order to keep the $y+$value around 2 as a requirement of the turbulence model.

The plots given in Figure 3 show that there is good qualitative agreement between the experimental and the numerical results. However, quantitatively there are small differences, especially

DOI: 10.1002/fld

Table I. Various grid sizes used for grid independence studies.

Grid no.	Points, on aerofoil i	Points, radial direction j	Points, spanwise k	First grid point distance	Grid size
1	125	70	45	$1\times10^{-4}c$	393 750
2	125	70	45	$3\times10^{-5}c$	393 750
3	125	100	45	$3\times10^{-5}c$	562 500
4	161	100	60	$3\times10^{-5}c$	966 000
5	232	90	60	3×10^{-5}c	1 252 800
6	300	100	60	$1\times10^{-5}c$	1 800 000

in the values of lift coefficient at higher angles of attack and during the downstroke motion of the wing; these are the regions of motion where the flow tends to separate. This small discrepancy is attributed to the use of the Baldwin–Lomax turbulence model. Keeping in view the qualitative nature of this study of the oscillating wing, the results are considered to be quite adequate with no flow separation detected, which is in accordance with the published work [12].

The various views of the finally selected grid are shown in Figure 4.

To carry out time marching, a non-dimensional time step of 0.004 was chosen after the time step sensitivity study based on the force coefficients. This non-dimensional time step corresponds to a physical time step of the order of 10^{-6} s. It is found that for the current selection, the time step had a very negligible effect on the force coefficient curves keeping in view the repeatability and accuracy of the results against published data. Results of only two different time steps are presented for the force coefficient curves in Figure 5. Similarly for the higher reduced frequencies the repeatability of the results was also checked against the time step.

3.4. Boundary conditions

For the boundary conditions, at the in-flow boundary, the velocity components and temperature are specified, while the pressure is extrapolated from the interior. Outflow is defined by fixing the pressure equal to the free-stream static pressure and extrapolating the velocity and temperature from the interior. Along the grid cut-line, periodic boundary conditions were enforced. On points of the inner boundary, adiabatic, impermeable wall and no-slip boundary conditions were applied. At the slit outboard of the wing tip, the flow quantities are averaged from both sides of the plane, while a symmetric boundary condition is used at the wing root as half the wing (semispan) is modeled.

4. RESULTS AND DISCUSSION

The three cases with reduced frequency (k), 0.1, 0.2 and 0.3, have been compared to see the effect of the changing reduced frequency on the oscillating wing with the help of force coefficients, pressure distribution and flow visualization. The results of the first case have been compared in detail with the published work [12] as already described. The other two cases being newer in scope could not be compared due to the unavailability of the data. However, the experimental validation of these cases is necessary only if some irregular characteristic behavior is observed. The results of

DOI: 10.1002/fld

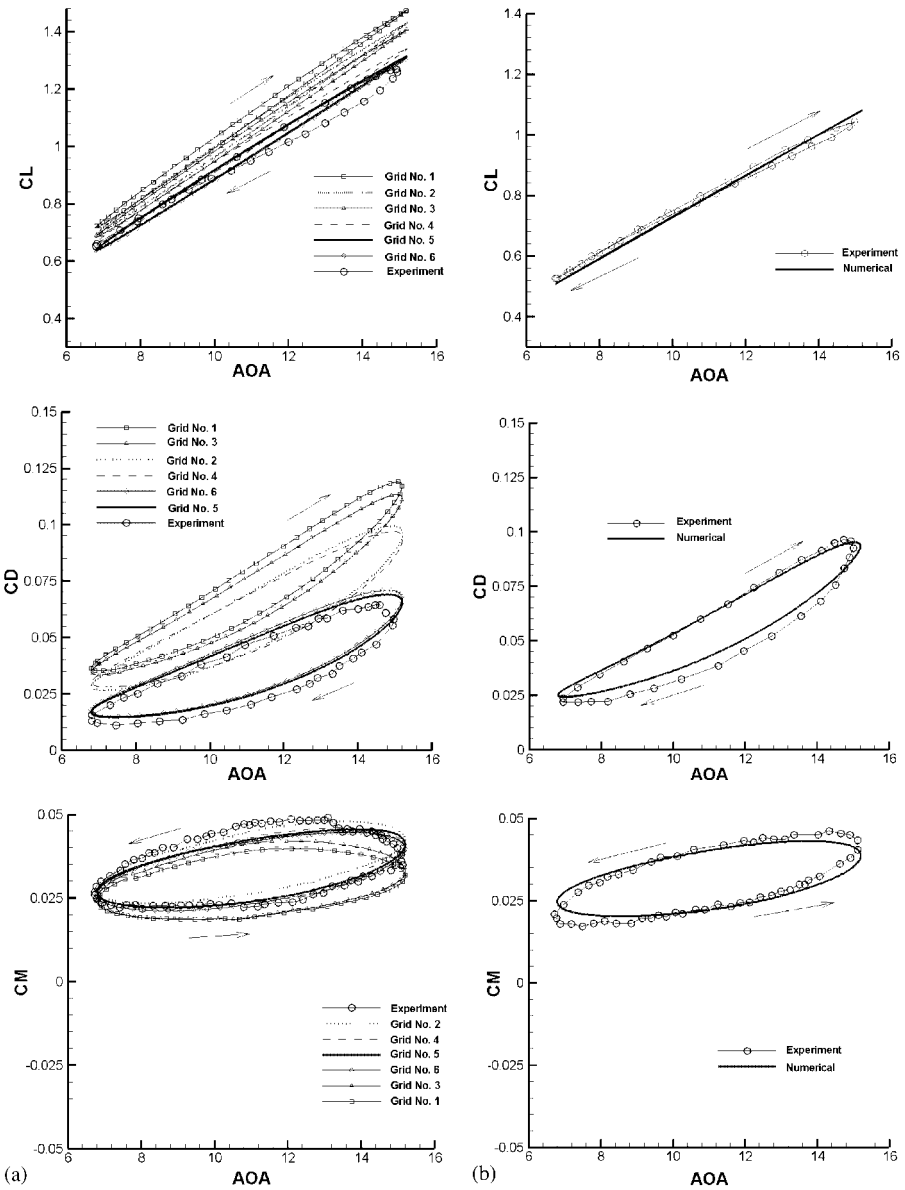

Figure 3. (a) Grid independence and validation: plots of lift, drag and moment coefficients *vs* AOA at 47.5% span location. Experimental data from Piziali [12]. $\alpha = 11 + 4.2\sin(2M_\infty k\tau)$, $M_\infty = 0.299$, $Re = 1\,990\,000$, $k = 0.10$. (b) Plots of lift, drag and moment coefficients *vs* AOA at 80% span location. Experimental data from Piziali [12]. $\alpha = 11 + 4.2\sin(2M_\infty k\tau)$, $M_\infty = 0.299$, $Re = 1\,990\,000$, $k = 0.10$. (c) Plots of lift and moment coefficients *vs* AOA at 90% span location. Experimental data from Piziali [12]. $\alpha = 11 + 4.2\sin(2M_\infty k\tau)$, $M_\infty = 0.299$, $Re = 1\,990\,000$, $k = 0.10$. (d) Plots of lift, drag and moment coefficients *vs* AOA at 95% span location. Experimental data from Piziali [12]. $\alpha = 11 + 4.2\sin(2M_\infty k\tau)$, $M_\infty = 0.299$, $Re = 1\,990\,000$, $k = 0.10$.

DOI: 10.1002/fld

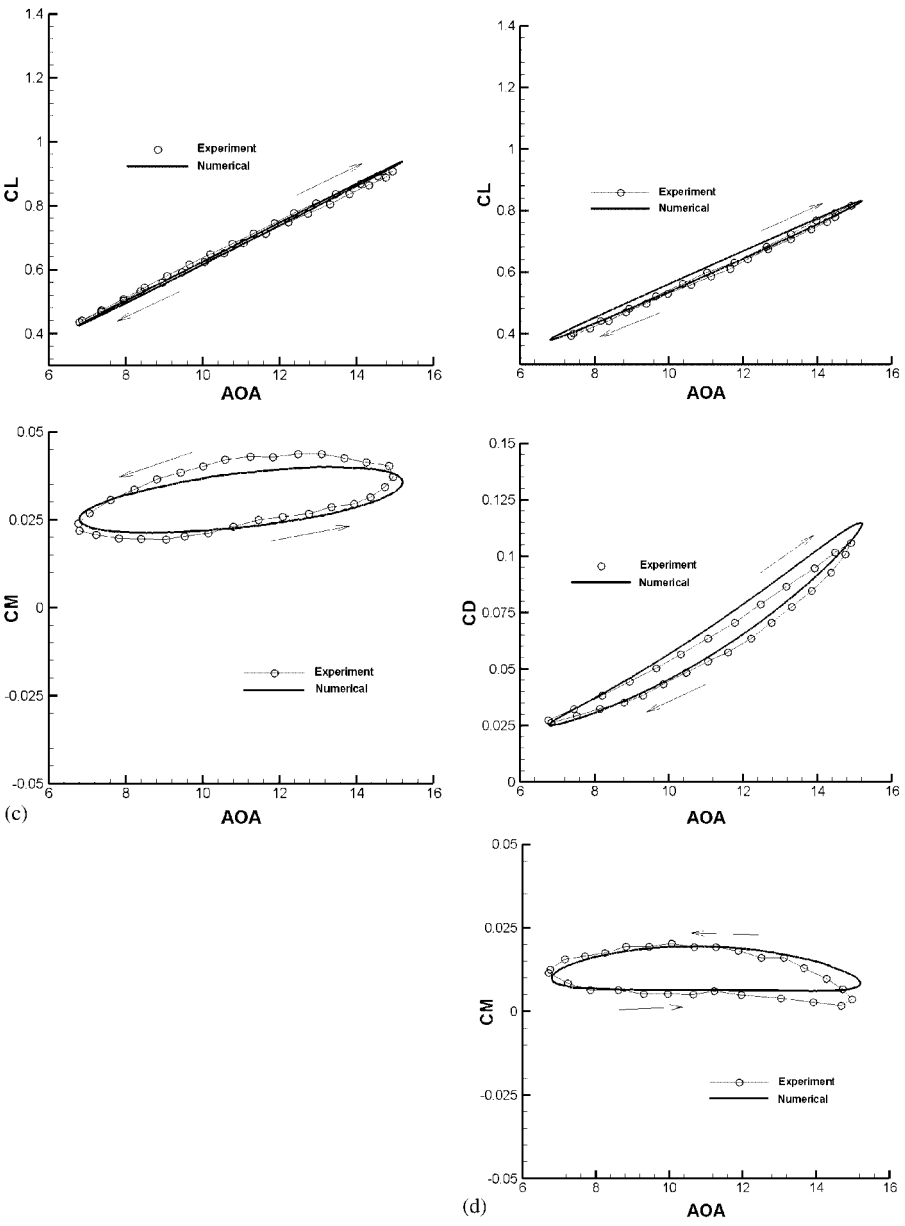

Figure 3. *Continued*.

all the cases have been presented in the form of various flow pictures and plots. The flow pictures of various quantities are provided at instances near the maximum amplitude location as the area of prime concern at 15° during the upstroke and at the same instance during the downstroke. Various types of plots include streamlines, velocity vector plots and vorticity contour plots, force

DOI: 10.1002/fld

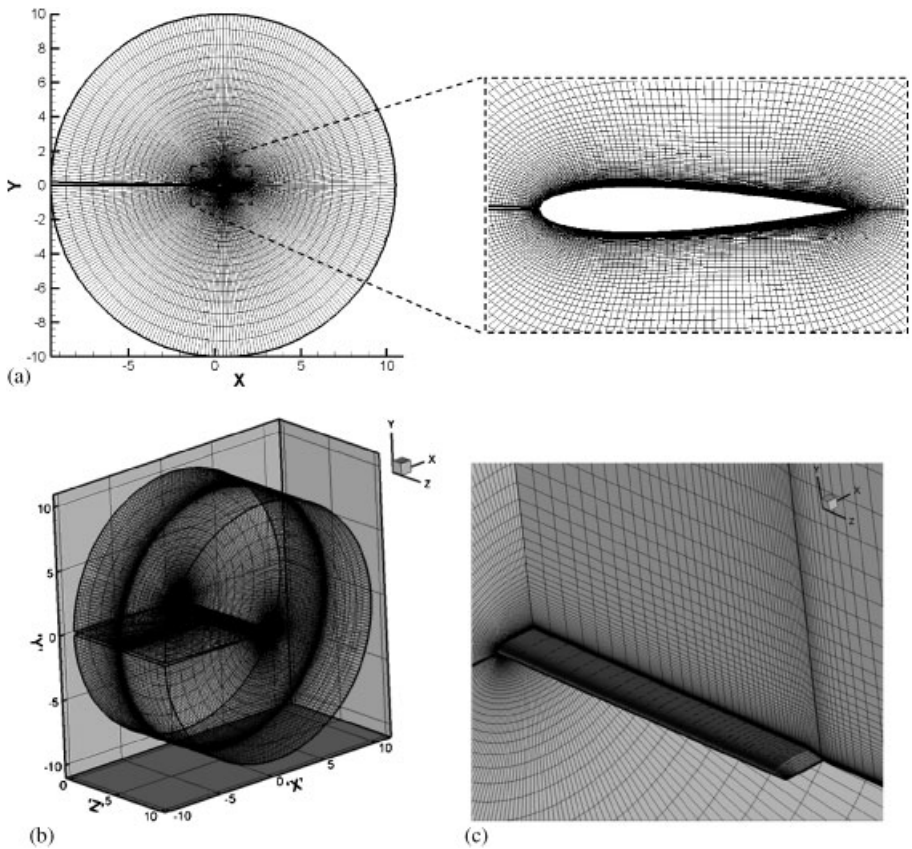

Figure 4. A 3D grid for semispan AR = 5, NACA 0015 wing showing (a) section 2D grid; (b) 3D perspective view; and (c) internal view of the grid.

coefficient plots and pressure distributions. The flow pictures are presented at span locations of 47.5, 80, 90 and 95% as shown in Figure 6. These locations are indicated by 'a, b, c and d,' respectively, in the subsequent figures for clear understanding.

Results of the force coefficients of the complete oscillation cycle are compared for the three reduced frequencies in Figure 7. These results are presented at various span locations on the semispan wing from midspan toward the tip as described above. The arrows show the directions of the upstroke and the downstroke. The lift coefficient, see (*plots a1–d1* in figure), with the increase in α increases gradually and *vice versa*.

The slopes and the magnitudes of the lift curves, however, decrease in the spanwise direction from midspan toward the tip. These curves for all the reduced frequencies lie over each other in all the plots almost around a mean position. However, the hysteresis loops are of different magnitudes. For higher pitch rates the hysteresis loop is bigger. The moment curves (*plots a3–d3* in figure) also show a similar behavior as the lift curves. They all vary in a similar manner with respect to each other, with changing α. Their variation from midspan toward the tip is also similar to the previous behavior of lift curves, while the drag curves (*plots a2–d2* in figure) have a larger

DOI: 10.1002/fld

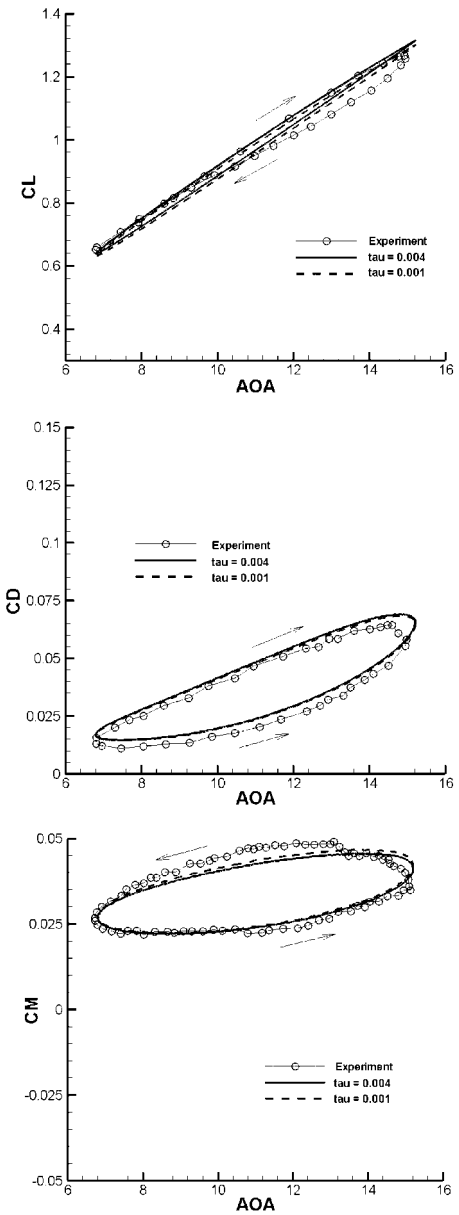

Figure 5. Variation in time steps: plots of force coefficient *vs* AOA at 47.5% span location. Experimental data from Piziali [12], $\alpha = 11 + 4.2\sin(2M_\infty k\tau)$, $M_\infty = 0.299$, $Re = 1\,990\,000$, $k = 0.10$.

magnitude and slopes near the tip compared with the midspan. However, they also lie around a mean position like the other force curves. Another interesting feature observed from the above-mentioned figures is that the magnitude of force coefficients, especially the lift coefficient, toward the wing tip at any instant of time decreases gradually with a lesser magnitude compared with

DOI: 10.1002/fld

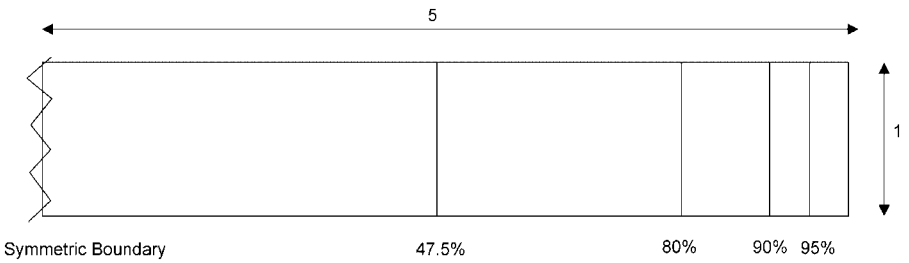

Figure 6. Location of spanwise stations on the wing.

midspan locations, which is not very similar to static cases. This is because of finite time taken by the tip vortex to form, thus inducing a lag in the response of the tip vortex to the wing loading. A possible consequence of these factors is that, as the pitch rate increases, the spanwise loading distribution may become flatter and the magnitude of the induced incidence at any spanwise location would reduce [9]. The above-mentioned trends can also be seen in total force coefficient plots in Figure 8.

The primary effect of the increasing pitch rate is to restrain the forward movement of the trailing edge separation point. This results in an extension of the linear portion of the normal force or lift coefficient curve. In all the cases there has been less overshoot of the linear portion of the curve. Furthermore, under the given conditions since there has been no DS effect and subsequent separation, in all the cases the maximum lift coefficient is nearly the same at maximum α. The additional lift is obtained as a result of the dynamic motion of the wing. Hysteresis is present in all the three force coefficients of dynamic cases and is much more severe at higher oscillation frequencies. The higher reduced frequency gives the flow little chance to re-establish itself. Hence, during the downstroke the flow remains mostly less energized; thus there is a significant hysteresis between upstroke and downstroke.

A comparison of the force coefficients has given a fair idea of the differences among the three cases studied with different pitch rates. The review and analysis of the lift, drag and pitching moment data give a global view of the unsteady flow response of a wing or airfoil undergoing the dynamic motion. However, the local flow behavior such as flow separation, etc. cannot be taken out and properly understood from the force and moment data. From an examination of the instantaneous pressure distribution, the flow separation characteristics, if any, can be figured out especially from the suction pressures. The leading or trailing edge separations or vortex formation phenomena can also be inspected. In the study it is found that the trends of all the cases are similar as there have been no ridges or abruptness, etc. in the pressure curves at all α. Suction pressures decrease from the leading edge toward the trailing edge and the distribution is smooth. In addition, it is smooth in the spanwise direction as well. α, 15° is chosen in a cycle, which is close to the maximum amplitude position of 15.2° in order to see the pressure distribution of the three cases. Results for the first case are shown for both the upstroke and the downstroke in Figure 9(a) and (b), respectively, where the non-dimensional pressures are plotted at various span stations.

During the upstroke, all the pressure curves are smooth with no abrupt changes indicating the smooth behavior of the flow. From the midspan toward the tip the distribution is shrinking and the difference between the upper and lower curve is decreasing, explaining the presence of lesser

DOI: 10.1002/fld

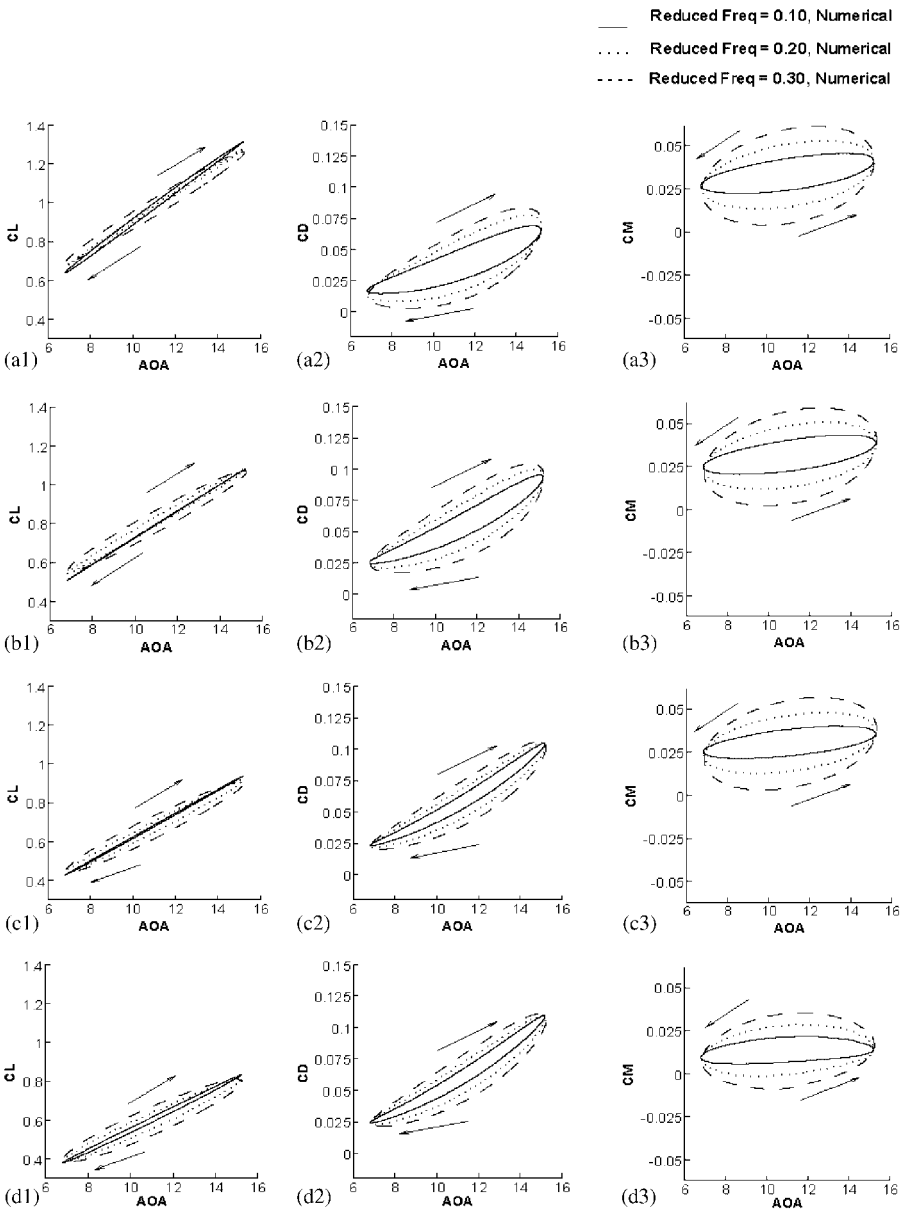

Figure 7. Sectional force coefficient plots for AR = 5, semispan NACA 0015 wing at 47.5, 80, 90 and 95% span locations for a complete cycle, $k = 0.10, 0.20$ and 0.30, $M_\infty = 0.299$, $\alpha = 11 + 4.2\sin(2M_\infty k\tau)$, $Re = 1\,990\,000$.

lift near the tip. There are few differences between the pressure distribution curves' position and magnitude among the three reduced frequency cases. There is little difference among the values of lift coefficients at a single α and their behavior is similar in all the three reduced frequency

DOI: 10.1002/fld

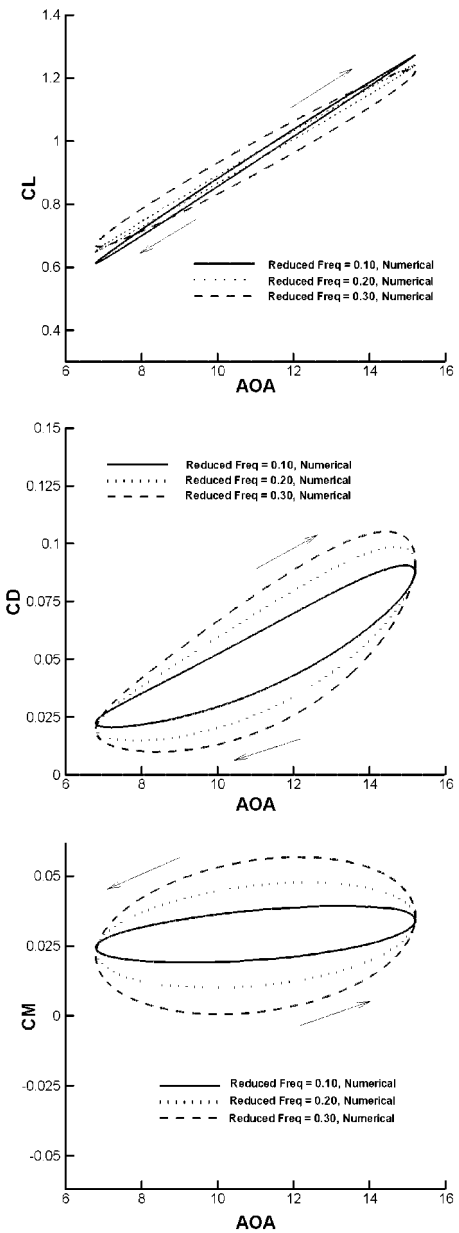

Figure 8. Total force coefficient plots for AR = 5, semispan NACA 0015 wing for complete cycle, $k = 0.10$, 0.20 and 0.30, $M_\infty = 0.299$, $\alpha = 11 + 4.2\sin(2M_\infty k\tau)$, $Re = 1\,990\,000$.

cases. During the downstroke the pressure distribution plot size is lesser than during the upstroke. That is why there is less lift during the downstroke at any single α. In addition, among the three frequencies, there is little difference between the magnitudes of the curves during the downstroke

DOI: 10.1002/fld

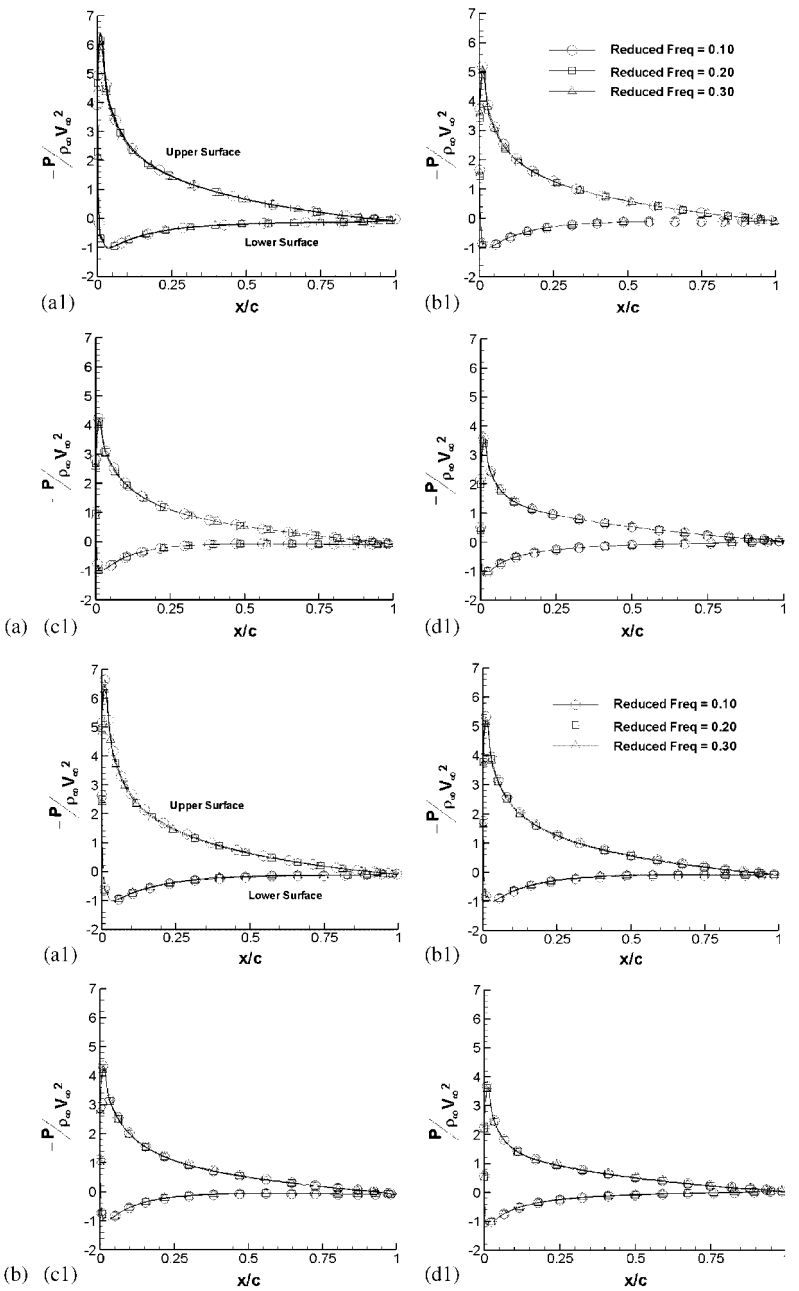

Figure 9. (a) Non-dimensional pressures at 47.5, 80, 90 and 95% span locations at 15° upstroke, $k=0.10$, 0.20 and 0.30, $M_\infty=0.299$, $\alpha=11+4.2\sin(2M_\infty k\tau)$, $Re=1\,990\,000$. (b) Non-dimensional pressures at 47.5, 80, 90 and 95% span locations at 15° downstroke, $k=0.10, 0.20$ and 0.30, $M_\infty=0.299$, $\alpha=11+4.2\sin(2M_\infty k\tau)$, $Re=1\,990\,000$.

DOI: 10.1002/fld

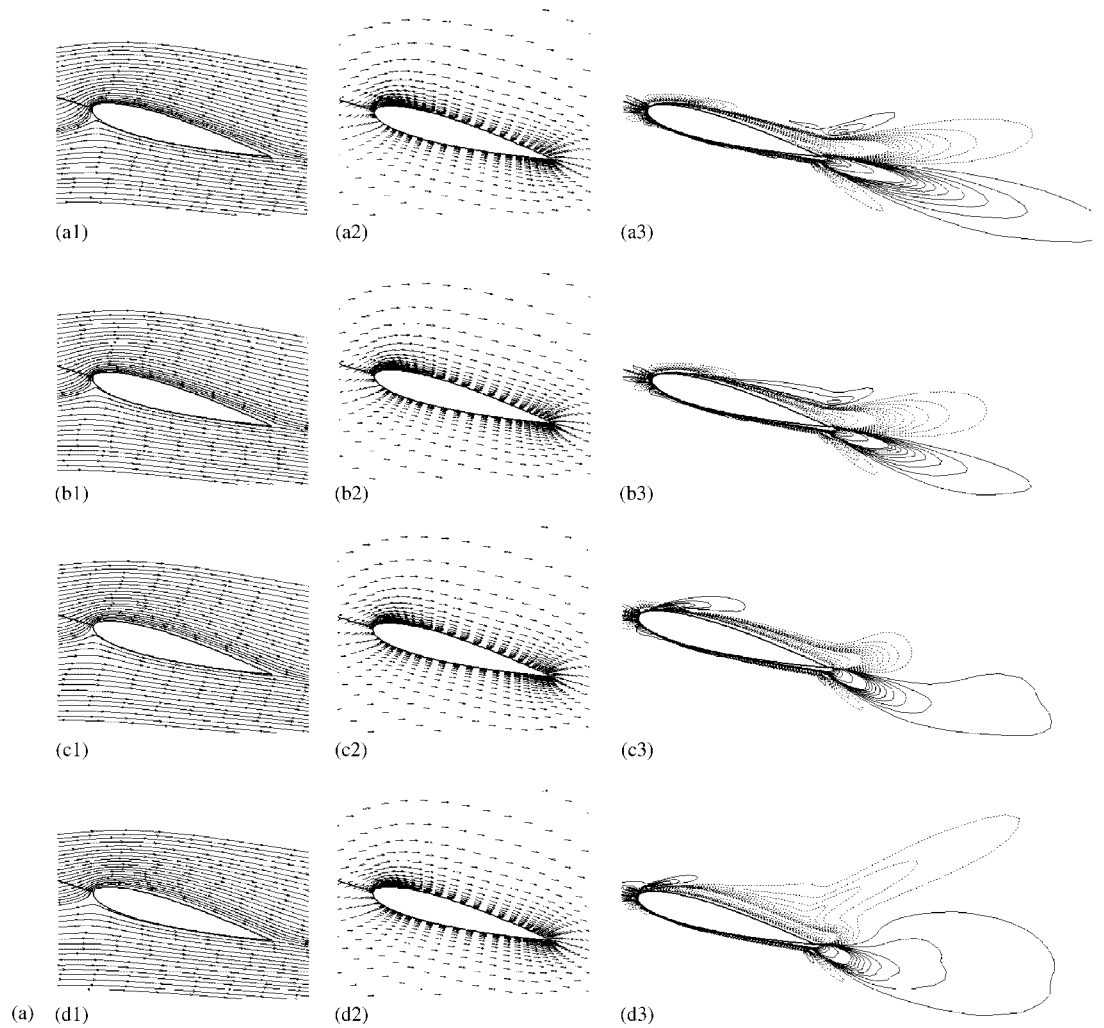

Figure 10. (a) Streamlines, velocity vectors and vorticity plots at 47.5, 80, 90 and 95% span locations at 15° upstroke, $k=0.10$, $M_\infty=0.299$, $\alpha=11+4.2\sin(2M_\infty k\tau)$, $Re=1\,990\,000$. (b) Streamlines, velocity vectors and vorticity plots at 47.5, 80, 90 and 95% span locations at 15° downstroke, $k=0.10$, $M_\infty=0.299$, $\alpha=11+4.2\sin(2M_\infty k\tau)$, $Re=1\,990\,000$.

and during the upstroke. Therefore, from the pressure distribution curves of all the cases, it is clear that they are smooth and there are no ridges (no presence of separation vortices). In all the cases the suction peak pressures at the leading edge have no abrupt drop throughout the respective oscillating cycles. The flow is smooth and attached. The variation in a single plot among the three reduced frequencies' pressure distribution is small but once this distribution is integrated over the whole surface, the difference in the values of force coefficients becomes more evident as is already shown in the force coefficient plots.

DOI: 10.1002/fld

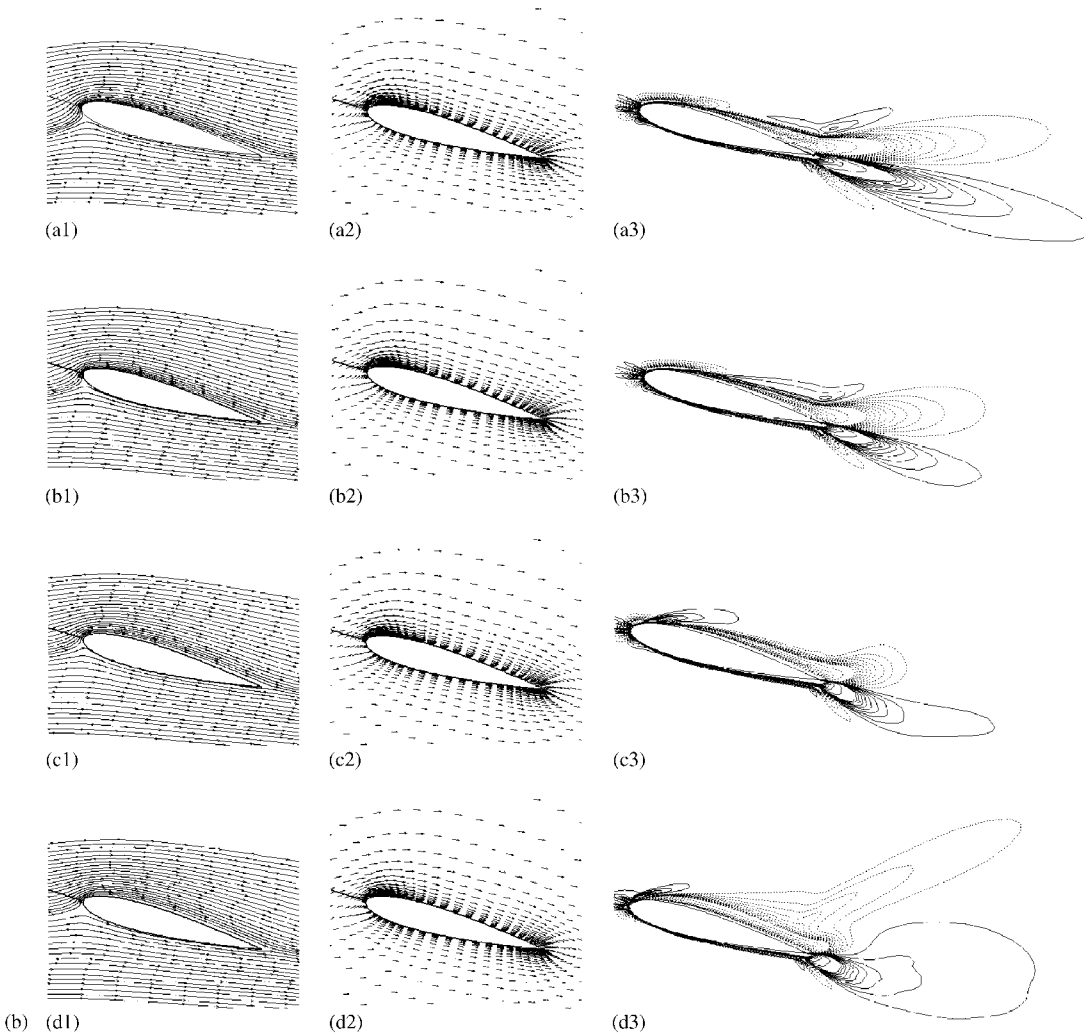

Figure 10. *Continued*.

Similar to the pressure distribution the flow pictures are provided as well to ascertain the flow behavior for the varying reduced frequency. From the flow pictures it is again enforced that at the given conditions throughout the angle of attack range, for all the cases, the flow remains attached to the surface with no flow reversals, separation, etc. Similar to the pressure distribution plots, at α of 15°, the streamlines, velocity vectors and vorticity contours are plotted at the specific spanwise locations during both the upstroke and the downstroke in a motion cycle. All the vorticity contours for comparison purposes are on the scale of -15 to 15, where the minimum contour levels are -0.1 and 0.1. In the 2D view for the vorticity contours, the negative (clockwise, CW) and positive (counter clockwise, CCW) are represented as broken and solid lines, respectively. This spanwise vorticity is the z-component of the vorticity (ω_z). The response of all the cases is similar; hence, the flow pictures are provided for the first case in Figure 10(a) and (b).

DOI: 10.1002/fld

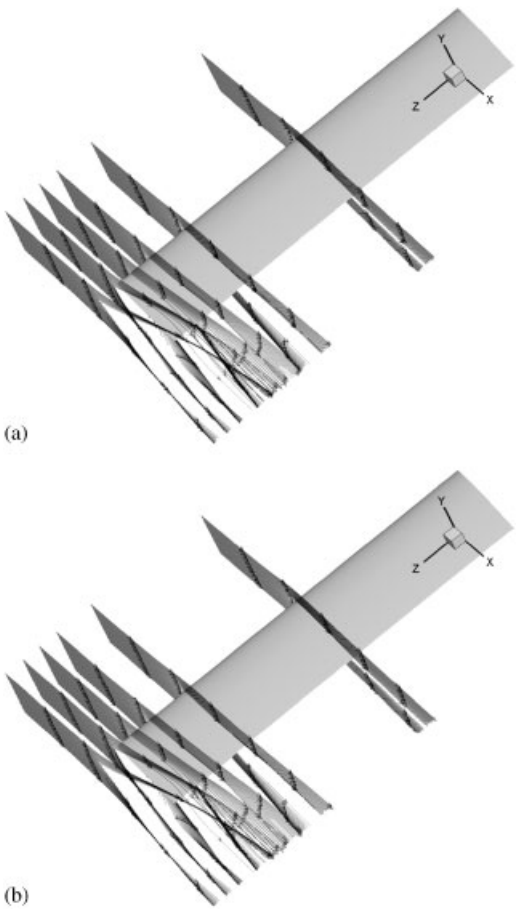

Figure 11. (a) 3D pathlines on AR = 5 semispan wing at 47.5, 80, 90, 95, 100 and 105% span locations at 15° upstroke, $k = 0.10$, $M_\infty = 0.299$, $\alpha = 11 + 4.2\sin(2M_\infty k\tau)$, $Re = 1\,990\,000$. (b) 3D pathlines on AR = 5 semispan wing at 47.5, 80, 90, 95, 100 and 105% span locations at 15° downstroke, $k = 0.10$, $M_\infty = 0.299$, $\alpha = 11 + 4.2\sin(2M_\infty k\tau)$, $Re = 1\,990\,000$.

It is apparent that the flow is regular; there is no flow reversal, etc. hence no separation. No vortices can be seen as well. The flow close to the wing exhibits the typical boundary layer pattern in all the cases with no sign of separation. The negative CW vorticity over the wing and CCW positive vorticity under the wing can be observed in Figure 10 (plots *a3–d3* in each figure) during the upstroke and the downstroke. At any single α the vorticity lines are closely packed indicating strong layers of vorticity (CW on the upper surface and CCW on the lower surface) in the midspan compared with the outboard locations near the tip, which explains the presence of more lift inboard compared with the outboard. This is again related to the downwash effect as already explained in force curve plots.

The facts narrated above can be more easily comprehended by looking at the 3D flow pictures. For the same α of 15°, 3D pathlines are shown in Figure 11(a) and (b) at the above-mentioned

DOI: 10.1002/fld

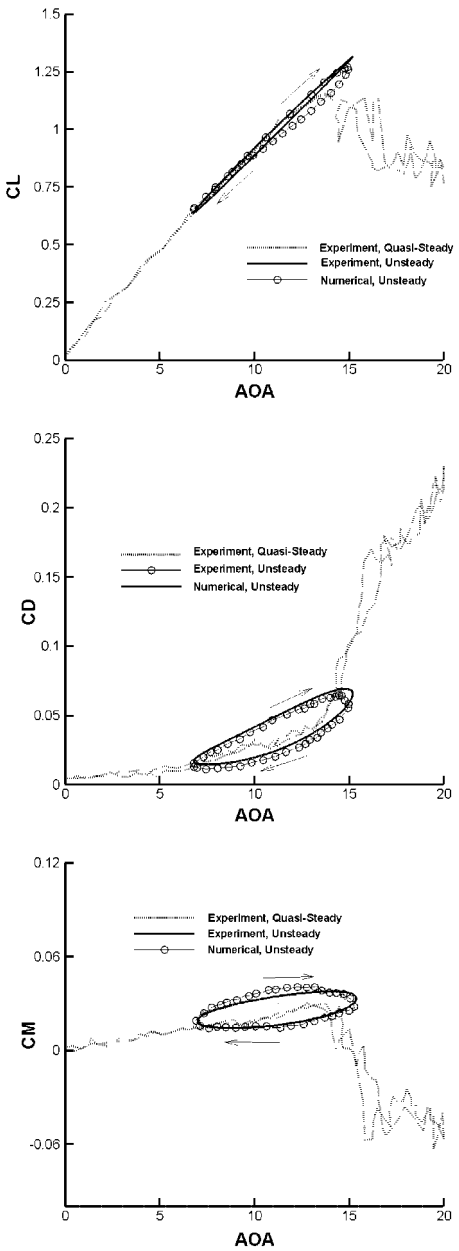

Figure 12. Plots of lift, drag and moment coefficients *vs* AOA at 47.5% span location. Experimental data from Piziali [12], $M_\infty = 0.299, Re = 1990000$. Unsteady motion: $k = 0.10$, $\alpha = 11 + 4.2\sin(2M_\infty k\tau)$. Quasi-steady motion: $k = 0.000$, $\alpha = 10 + 10\sin(2M_\infty k\tau)$.

DOI: 10.1002/fld

spanwise stations and additional stations located at 100 and 105%. The tip vortex is clearly captured during the upstroke and the downstroke motions. The flow in the vicinity of the tip can be clearly observed as going from the bottom of the wing toward the upper surface near the tip. For the flow conditions in this study, the distinctive DSV is not observed as already described in the above discussion; hence, the formation of the typical *omega* vortex (due to the interaction between the resident tip vortex and the time-evolved DSV) as explained by some researchers [22, 23, 40] is not observed. This is primarily due to the relatively lower values of mean α and amplitude of motion.

The static and DS processes are compared in Figure 12 where the experimental and numerical simulation results are plotted. The mean angle of attack of 11° for the unsteady motion is near the static stall angle and hence the amplitude of the motion increases the angle to 15.2°. Even at post-static stall angles there is considerable lift and moment. Similarly, there is no abrupt drag rise or sudden negative pitching moment indicating no or very light category DS.

5. CONCLUSION

Numerical simulation for a high Reynolds number at unsteady 3D flow field over an oscillating wing has been undertaken. Based on the results, the following conclusions are drawn:

(a) Under the given conditions for all the reduced frequency values, force coefficient curves, the surface pressure distribution and flow visualization indicate that the flow remains attached to the wing surface with no clear separation or typical light-to-deep category DS.
(b) Hysteresis is present in the force coefficients and is much more severe at higher reduced frequencies. The increase in pitch rate has resulted in higher gradients, which is in line with the studies performed by previous authors.
(c) The maximum lift coefficient is nearly the same for all the reduced frequency values at maximum α.
(d) The magnitude of the force coefficients and especially the lift coefficient near the wing tip at any instant of time does not decrease much compared with midspan locations, which is not similar to static cases where near the wing tips less force is produced due to 3D effects.

The code has been successfully validated to undertake similar studies involving unsteady motion. Subsequent research is focused on adding newer turbulence models to the code besides its application to the challenging area of flow control for 3D wings.

NOMENCLATURE

2D	two-dimensional
3D	three-dimensional
a_∞	free stream speed of sound
α	angle of attack
α_a	a constant defining maximum and minimum amplitude of pitching motion
α_m	mean angle of attack
AR	aspect ratio
c	chord length
CW	clockwise

DOI: 10.1002/fld

CCW	counter clockwise
CFD	computational fluid dynamics
CL	coefficient of lift
CD	coefficient of drag
CM	coefficient of pitching moment
DSV	dynamic stall vortex
i	grid coordinate on the airfoil surface
j	grid coordinate in the radial direction
k	grid coordinate in spanwise direction
k	reduced frequency, $k=\omega c/2u_\infty$
M_∞	free stream Mach number
N–S	Navier–Stokes
Re	Reynolds number
τ	tau, non-dimensional time
t	time
u_∞	free stream velocity
ω	angular velocity
ω_z	spanwise component of vorticity
μ	viscosity of the fluid
X, Y, Z	coordinates in the inertial frame of reference
∞	free stream condition

REFERENCES

1. McCroskey WJ. Unsteady airfoils. *Annual Review of Fluid Mechanics* 1982; **14**:285–311.
2. McCroskey WJ. The phenomenon of dynamic stall. *NASA TM-81264*, 1981.
3. Farren WS. The reaction on a wing whose angle of attack is changing rapidly. *Reports R&M 1648*, Air Ministry Aeronautical Research Committee, Great Britain, 1935.
4. McCroskey LW, Carr LW, McAlister KW. Dynamic stall experiments on oscillating airfoils. *AIAA Journal* 1976; **14**(1):57–63.
5. McCroskey KW, McAlister KW, Carr LW, Pucci SL. An experimental study of dynamic stall on advanced airfoil sections. *NASA TM 84245*, 1982.
6. McAlister KW, Carr LW, McCroskey WJ. Dynamic stall experiments on the NACA-0012 airfoil. *NASA Technical Paper 1100*, 1978.
7. Carr LW. Progress in analysis and prediction of dynamic stall. *Journal of Aircraft* 1988; **25**(1):6–17.
8. Ekaterinaris JA, Platzer MF. Computational prediction of airfoil dynamic stall. *Progress in Aerospace Sciences* 1996; **32**(6):523–573.
9. Lorber PF, Covino Jr AF, Carta FO. Dynamic stall experiments on swept three dimensional wing in compressible flow. *AIAA Paper 1795*, January 1991.
10. Lorber PF. Compressibility effects on the dynamic stall of a three dimensional wing. *AIAA Paper 0191*, January 1992.
11. Schreck SJ, Helin HF. Unsteady vortex dynamics and surface pressure topologies on a finite wing. *Journal of Aircraft* 1994; **31**(4):899–907.
12. Piziali RA. 2-D and 3-D oscillating wing aerodynamics for a range of angles of attack including stall. *NASA TM 4632*, September 1994.
13. Tang DM, Dowell EH. Experimental investigation of three dimensional dynamic stall models oscillating in pitch. *Journal of Aircraft* 1995; **32**(5):163–186.
14. Coton FN, Galbraith RAM. An examination of dynamic stalling of two wing planforms. *Aerospace Engineering Report 9526*, Department of Aerospace Engineering, University of Glasgow, Glasgow, Scotland, U.K., 1995.
15. Moir S, Coton FN. An experimental study of dynamic stall on a finite wing. *Aeronautical Journal* 1999; **103**(1023):229–236.

DOI: 10.1002/fld

16. Berton E, Allain C, Favier D, Maresca C. Experimental methods for subsonic flow measurements. In *Progress in Computational Flow–Structure Interaction*, Chapter 2.10, Hasse W, Selmin V, Winzell B (eds). Notes on Numerical Fluid Mechanics and Multidisciplinary Design, vol. 81. Springer: Berlin, 2003.
17. Berton E, Allain C, Favier D, Maresca C. Database for steady and unsteady 2-d and 3-d flow. In *Progress in Computational Flow–Structure Interaction*, Chapter 3.2, Hasse W, Selmin V, Winzell B (eds). Notes on Numerical Fluid Mechanics and Multidisciplinary Design, vol. 81. Springer: Berlin, 2003.
18. Newsom RW. Navier–Stokes simulation of wing–tip and wing–juncture interactions for a pitching wing. *AIAA 2259*, June 1994.
19. Ekaterinaris JA. Numerical investigation of dynamic stall on an oscillating wing. *AIAA 0781*, January 1995.
20. Ekaterinaris JA. Numerical investigation of dynamic stall on an oscillating wing. *AIAA Journal* 1995; **33**(10): 1803–1808.
21. Morgan PE, Visbal MR. Simulation of unsteady three dimensional separation on a pitching wing. *AIAA 2709*, June 2001.
22. Spentzos A, Barakos G, Badcock K, Richards B. CFD study of 3-D dynamic stall. *AIAA 1107*, January 2005.
23. Spentzos A, Barakos G, Badcock K, Richards B, Wernert P, Schreck S, Raffel M. Investigation of 3-D dynamic stall using computational fluid dynamics. *AIAA Journal* 2005; **43**(5):1023–1033.
24. Liu JC, Sun M, Wu LY. Navier–Stokes analysis of circulation control airfoil. *Acta Mechanica Sinica* 1995; **11**:137–143.
25. Sheikh S. A study on the mechanism and control of dynamic stall on an airfoil. *Ph.D. Dissertation*, Beijing University of Aeronautics and Astronautics (BUAA), China, February 1998.
26. Sun M, Sheikh S. Dynamic stall suppression on an oscillating airfoil by steady and unsteady tangential blowing. *Aerospace Science and Technology* 1999; **3**(6):355–366.
27. Hamdani HR. A study of the mechanisms of high-lift generation by airfoil and wing at small Reynolds number. *Ph.D. Dissertation*, Beijing University of Aeronautics and Astronautics (BUAA), China, March 2000.
28. Sun M, Hamdani HR. Separation control by alternating tangential blowing/suction at multiple slots. *AIAA 0297*, 2001.
29. Riaz R. Effects of different thickness variation strategies on dynamic stall in an oscillating airfoil. *M.S. Thesis*, College of Aeronautical Engineering, National University of Sciences and Technology (NUST), Pakistan, 2004.
30. Naqvi A. Force generation and flow at low Reynolds number during hovering motion. *M.S. Thesis*, PAF College of Aeronautical Engineering, National University of Sciences and Technology (NUST), Pakistan, 2005.
31. Hamdani HR, Riaz R, Qureshi H *et al*. Effects of different thickness variation strategies on dynamic stall in an oscillating airfoil. *Third AIAA Flow Control Conference*, San Francisco, U.S.A., 2006; AIAA 3691.
32. Umar F. Effect of various reduced frequencies on an oscillating wing. *M.S. Thesis*, College of Aeronautical Engineering, National University of Sciences and Technology (NUST), Pakistan, 2006.
33. Umar F, Hamdani HR *et al*. Numerical investigation of the effect of reduced frequencies for helicopter rotor application. *Fifth International Bhurban Conference on Applied Sciences and Technology* (*IBCAST*), Islamabad, Pakistan, 8–11 January 2007.
34. Umar F, Naqvi A, Hamdani HR *et al.* Simulation of insect flight—hovering motion at low Reynolds number. *Fifth International Bhurban Conference on Applied Sciences and Technology* (*IBCAST*), Islamabad, Pakistan, 8–11 January 2007.
35. Steger JL. Implicit finite-difference simulation of flow about arbitrary two-dimensional geometries. *AIAA Journal* 1978; **16**:679–696.
36. Beam RM, Warming RF. An implicit factored scheme for the compressible Navier–Stokes equations. *AIAA Journal* 1978; **16**:393–402.
37. Baldwin BS, Lomax H. Thin layer approximation and algebraic model for separated flows. *AIAA 257*, 1978.
38. Rizzeta DD, Visbal MR. Comparative study of two turbulence models for airfoil static and dynamic stall. *AIAA Journal* 1993; **31**:784–786.
39. Baldwin BS, Barth TJ. A one-equation turbulence transport model for high Reynolds number wall-bounded flows. *NASA TM 102847*, 1990.
40. Freymuth P. Three-dimensional vortex systems of finite wings. *Journal of Aircraft* 1988; **25**(10):971–972.

DOI: 10.1002/fld